Petroleum Science 23 (2026) 1986–2001

Contents lists available at ScienceDirect

Petroleum Science

journal homepage: www.keaipublishing.com/en/journals/petroleum-science

Original Paper

Research on the intelligent characterization of interwell section architecture based on Bayesian expert systems

De-Gang Wu[a,b,c], Sheng-He Wu[b,c,*], Zhen-Hua Xu[b,c], Lei Liu[a,b,c], Ming-Cheng Liu[b,c]

[a] *College of Artificial Intelligence, China University of Petroleum (Beijing), Beijing, 102249, China*
[b] *College of Geosciences, China University of Petroleum (Beijing), Beijing, 102249, China*
[c] *State Key Laboratory of Petroleum Resources and Engineering, China University of Petroleum (Beijing), Beijing, 102249, China*

ARTICLE INFO

Article history:
Received 12 July 2025
Received in revised form
5 January 2026
Accepted 28 January 2026
Available online 3 February 2026

Edited by Meng-Jiao Zhou

Keywords:
Bayesian inference
Interwell architectural characterization
Expert system
Uncertainty evaluation

ABSTRACT

The characterization of interwell section architecture is critical for revealing reservoir lateral heterogeneity and connectivity. This process integrates well and seismic data with geological knowledge yet faces inherent multiple solutions. Current characterization methods remain hampered by high levels of manual intervention, insufficient automation, and difficulties in evaluating the uncertainty of interwell section architecture. To address these challenges, this study presents an intelligent method for the automated characterization of reservoir architecture along section directions based on a Bayesian expert system. The approach quantifies domain knowledge via prior normal distributions. By utilizing well and seismic data, Bayesian probabilistic reasoning infers the guiding influence of each individual piece of domain knowledge on predicting the interwell distribution of architectural elements. A weighted ensemble decision framework then integrates these inferences to determine the interwell distributions of architectural elements and associated uncertainties. Case studies demonstrate that the method effectively evaluates uncertainty, generates geologically consistent section characterizations, achieves 81% consistency in blind well sand body predictions, and excels in delineating the lateral boundaries and contact relationships of architectural elements.

1. Introduction

Reservoir architecture refers to the morphology, scale, orientation, and stacking relationships of reservoir units and flow barriers at different hierarchical levels (Wu, 2010). Research on reservoir architecture reveals the heterogeneity and connectivity characteristics of the internal reservoir structure across various scales, providing an essential geological foundation for refined reservoir development and exploitation of the remaining oil potential. Interwell section architectural analysis, which dissects the hierarchical level, scale, morphology, and other characteristics of subsurface architecture along connecting well sections, is a vital aspect of reservoir architecture research.

Interwell architectural analysis relies primarily on well logging, seismic, and production data. Under development well patterns, architectural dissection typically follows the principle of section-plane interaction (Xu et al., 2020). This involves generating architectural element distribution maps based on interpretations from closely spaced well patterns and establishing sand body distribution patterns, which are then used to interpret the geometric characteristics (e.g., scale) of architectural elements along interwell sections. However, when architectural spatial complexity is high, the geometric characteristics of elements within the same depositional environment can vary significantly (Miall et al., 2022; Kundu, 2023). Relying solely on well data makes accurate prediction of architectural element distributions challenging. Leveraging the high lateral resolution of seismic data, methods that combine well and seismic data for section characterization have emerged (Liu et al., 2024; Sun et al., 2024). These methods supplement multiwell analysis with techniques such as seismic waveform classification (Yuan et al., 2022), spectral decomposition (Huang et al., 2021), seismic attributes (Li et al.,

---

* Corresponding author.
E-mail address: reser@cup.edu.cn (S.-H. Wu).
Peer review under the responsibility of China University of Petroleum (Beijing).

https://doi.org/10.1016/j.petsci.2026.01.046

2023), and joint seismic inversion (Crepaldi et al., 2024) to aid in determining sand body stacking patterns, morphology, and connectivity, thereby reducing uncertainty in interwell section characterization. Notably, the vertical resolution of seismic data is relatively limited and often insufficient for characterizing sand body distributions at the level of sublayers or single layers. To address this, methods based on architectural patterns for interwell prediction have been proposed (Yue et al., 2007; Chen 2022). These methods establish prototype models (Yan et al., 2014) by referencing modern sediments, field outcrops, numerical simulations, or dissections of adjacent dense well patterns. Quantitative architectural patterns, such as the absolute scale of elements, relative elevation differences, and empirical aspect ratio (width-to-thickness ratio) formulas, are derived from these models (Kelly, 2006; Chen et al., 2020; Rajput and Pathak, 2025). The distribution of interwell architectural elements is then predicted by fitting these quantitative patterns to subsurface well data (Yu et al., 2004; Ibekwe et al., 2023; Qiao et al., 2023). Nevertheless, significant uncertainty persists in interwell architectural characterization under conditions of complex reservoir distributions, diverse architectural patterns, and limited existing data, necessitating uncertainty analysis of the characterization results. Existing interwell section characterization methods rely predominantly on interactive processing by domain experts utilizing data visualization software, resulting in high manual intervention, low efficiency, and difficulties in quantitatively evaluating the uncertainty of the outcomes. Consequently, there is an urgent need to develop intelligent methods for interwell architectural characterization.

Bayesian inference expert systems (Kim et al., 2023; Schulz et al., 2025) are intelligent frameworks built upon Bayesian theory that are capable of efficiently integrating uncertain knowledge and existing data for intelligent decision-making; they have been successfully applied in fields such as medicine and geology (Agar et al., 2019). This study introduces a Bayesian inference expert system into section architecture characterization, proposing an intelligent method for interwell architectural characterization based on this system. The method quantitatively represents domain knowledge using the Bayesian expert system and infers the distribution of interwell architectural elements, enabling automated characterization of interwell sections and evaluation of its uncertainty. This approach addresses the challenge of quantifying uncertainty in interwell section architecture, fills a gap in the research on automated and intelligent interwell characterization methods, significantly enhances characterization efficiency, and provides a transferable technical paradigm for oilfield development requiring urgent interwell architectural analysis. Future work can extend this method to 3D interwell architectural characterization, advancing reservoir characterization toward comprehensive intelligence.

The remainder of this article is organized as follows. Section 2 elaborates on the methodological rationale. Section 3 details the case study application and assesses its effectiveness. Section 4 critically examines the applicability and potential of the method. Section 5 presents the conclusions.

2. Methodology

The core objective of interwell architectural characterization is to delineate the hierarchy, scale, and morphology of architectural elements within a single chronostratigraphic unit (i.e., a single layer), leveraging well logs and seismic data. The scale attribute is quantified using a statistical absolute scale and aspect ratio; morphology is indicated by architectural element types; and hierarchy is inferred based on the aforementioned information, supplemented by seismic lithology inversion and relative elevation differences.

The Bayesian expert system-based interwell architecture characterization (BES-IAC) method proposed in this paper integrates this diverse architectural information into a Bayesian expert system. It enables quantitative fitting between architectural patterns and subsurface data through Bayesian inference to deduce interwell architectural element characteristics. This methodology comprises three key steps, as indicated by the blue arrows in Fig. 1. First, the domain geological knowledge is quantified via prior probability distributions. Second, knowledge is fit with data by calculating the Bayesian posterior probabilities of multiple knowledge sources using observed data. Finally, multiple knowledge sources are synergistically integrated through a weighted ensemble decision process to determine the hierarchy, scale, and morphology of architectural elements, thereby accomplishing interwell section architectural characterization.

2.1. Quantification method for knowledge

The quantitative representation of knowledge serves as the fundamental basis for knowledge inference. Following the aforementioned approach, this study introduces five types of knowledge to guide the interwell architectural characterization process: architectural element type, seismic lithology inversion, relative elevation difference, statistical sand body scale, and sand body aspect ratio.

Among these, the architectural element type is quantified via label encoding (Herdian et al., 2024), whereas seismic lithology inversion is represented as an inversion value matrix. The latter three types describe the spatial position and geometric parameter characteristics of geological bodies, typically exhibiting inherent uncertainty within statistical intervals. Given that most independent variables in geology and nature approximately follow a normal distribution, this study primarily employs the normal distribution function to characterize the statistical regularity features of geological bodies.

A normal distribution is conventionally denoted as $N(\mu, \sigma^2)$, representing a variable x with mean μ and standard deviation σ. Its probability density function (PDF) is expressed as f:

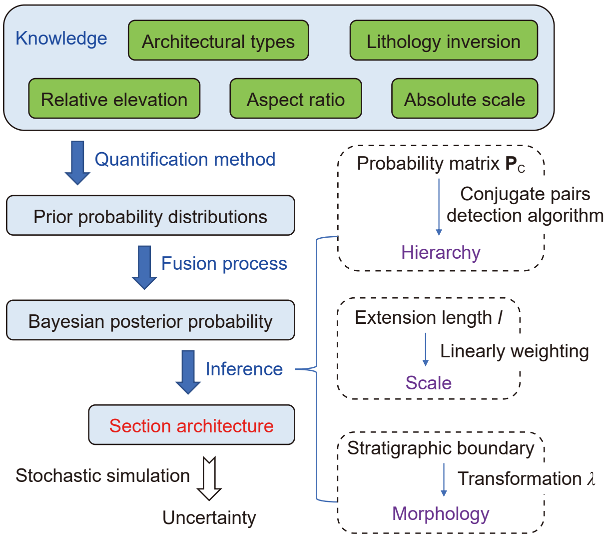

Fig. 1. Technical flowchart of the BES-IAC method.

$$f\left(x;\mu,\sigma^2\right) = \frac{1}{\sqrt{2\pi}\sigma}\exp\left(-\frac{(x-\mu)^2}{2\sigma^2}\right) \tag{1}$$

When statistical samples are available, the parameters of f may be estimated via maximum likelihood (Eliason et al., 1993); conversely, predefined statistical intervals can be utilized for parameter estimation. Considering that f possesses the characteristic $\int_{\mu-2\sigma}^{\mu+2\sigma} f(x)\mathrm{d}x \approx 0.9545$, where 95.45% of samples fall within the interval $[\mu-2\sigma, \mu+2\sigma]$ of approximately twice the standard deviation around the mean (Fig. 2), the parameters of f can be estimated using a geologically plausible interval $[x_\mathrm{L}, x_\mathrm{U}]$, where L stands for lower, and U stands for upper. Specifically, μ and σ are set as

$$\begin{cases} \mu = \dfrac{1}{2}(x_\mathrm{L} + x_\mathrm{U}) \\ \sigma = \dfrac{1}{4}(x_\mathrm{U} - x_\mathrm{L}) \end{cases} \tag{2}$$

2.2. Fusion process of knowledge and data

For an interwell section sequentially connecting K wells ($\{\mathrm{W}_1, \mathrm{W}_2, \cdots, \mathrm{W}_K\}$), the BES-IAC method infers the distribution of architectural elements between adjacent wells $<\mathrm{W}_k, \mathrm{W}_{k+1}>$ ($k = 1, 2, \cdots, K-1$) in sequence. A crucial foundation for determining the distribution of architectural elements between adjacent wells is the hierarchical division of individual sand bodies; only after hierarchical division can features such as the scale and morphology of architectural elements be determined.

This paper defines a pair of sand segments originating from the same individual sand body as a conjugate sand pair, establishing the relationship between two sand segments belonging to the same architectural element or architectural element combination as a conjugate relationship. The process of fitting knowledge and data involves calculating the posterior probability distribution of conjugate relationships between sand segments drilled through by adjacent wells, which is the conjugate probability, based on the prior probability distributions established by various knowledge sources and combined with observed data.

Let the sand segments drilled through by W_k and W_{k+1} be denoted as a and b, respectively (Fig. 3). The methods for constructing conjugate probability functions controlled by these five types of knowledge—architectural element type, relative elevation difference, statistical sand body scale, sand body aspect ratio, and seismic lithology inversion—are deduced below. Conditional probability and Bayesian probability are introduced for knowledge inference:

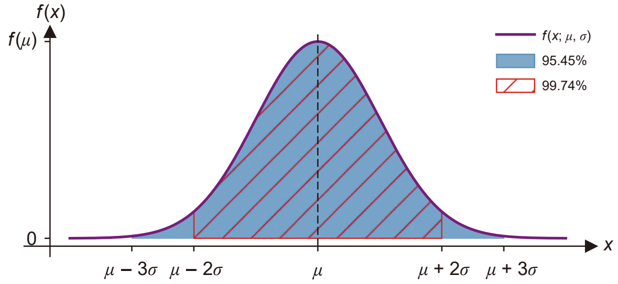

Fig. 2. Schematic diagram of the normal distribution function.

$$P(B|A) = \frac{P(AB)}{p(A)} \tag{3}$$

$$P(B|A) = \frac{P(A|B)P(B)}{P(A)} \tag{4}$$

2.2.1. Fitting of architectural element type

Architectural element types reflect sedimentary bodies formed by different genetic processes. Therefore, the primary consideration for determining a conjugate relationship between sand segments is the configuration relationship between their architectural element types. Let $\varphi(a,b) \in \{0,1\}$ represent the conjugate relationship indicator coefficient for a and b, characterizing their conjugate probability based solely on architectural element type.

For identical architectural element types of a and b, conjugate relationships may develop between them; hence, $\varphi(a,b) = 1$ is defined. When element types differ, the conjugate potential is determined by combinatorial rules of element types; that is, for architectural element types potentially forming a combination unit, $\varphi(a,b) = 1$ is defined. For example, in a fan-delta depositional system, distributary channels and mouth bars exhibit a genetic association. Due to the incising action of rivers on mouth bars, a spatial stacking pattern of “rivers incising and overlying mouth bars” is formed, as shown in Fig. 3(a) (Zhang et al., 2022). Conversely, for architectural element types with no specific configuration relationship, $\varphi(a,b) = 0$ is defined.

2.2.2. Fitting of the relative elevation difference

Relative elevation E refers to the elevation difference between a sand segment and the isochronous stratum in which it resides (Fig. 3(b)), reflecting the relative time of sand body formation, specifically, the hierarchical characteristic. The relative elevation difference z is an independent random variable that describes the difference in relative elevation between two sand segments and serves as a crucial indicator for determining the conjugate relationships between adjacent well sand segments.

Assume that z follows a uniform distribution, whereas the relative elevation difference ΔE of a conjugate sand pair follows a normal distribution $\Delta E \sim N(\mu_\mathrm{E}, \sigma_\mathrm{E}^2)$. From the Bayesian probability formula, it is known that $P(\mathrm{conjugate}|z = \Delta E) = P(z = \Delta E|\mathrm{conjugate})P(\mathrm{conjugate})/P(z = \Delta E)$. Considering that $P(z = \Delta E)$ and $P(\mathrm{conjugate})$ are unknown constants, it follows that $P(\mathrm{conjugate}|z = \Delta E)$ is linearly related to $P(z = \Delta E|\mathrm{conjugate})$. Therefore, for any sand segments a and b, their conjugate probability p_E controlled by the relative elevation difference is a linear mapping of the probability density $f_\mathrm{E}(z)$ of their relative elevation difference z, expressed as

$$p_\mathrm{E}(z) = k_\mathrm{E} f_\mathrm{E}(z) + b_\mathrm{E} \tag{5}$$

To effectively determine the scaling factor k_E and the bias b_E, considering the nonnegativity and convergence of p_E, the conditions $p_\mathrm{E}(z) \geq 0$ and $\lim\limits_{z\to\infty} p_\mathrm{E}(z) = 0$ should hold. When the relative elevation difference equals the mean μ_E, the sand pair has the maximum conjugate probability, specifically, $p_\mathrm{E}(\mu_\mathrm{E}) = k_\mathrm{E}\left(\sqrt{2\pi}\sigma_\mathrm{E}\right)^{-1} + b_\mathrm{E} = 1$. Based on this, the solution is

$$\begin{cases} k_\mathrm{E} = \sqrt{2\pi}\sigma_\mathrm{E} \\ b_\mathrm{E} = 0 \end{cases} \tag{6}$$

Thus,

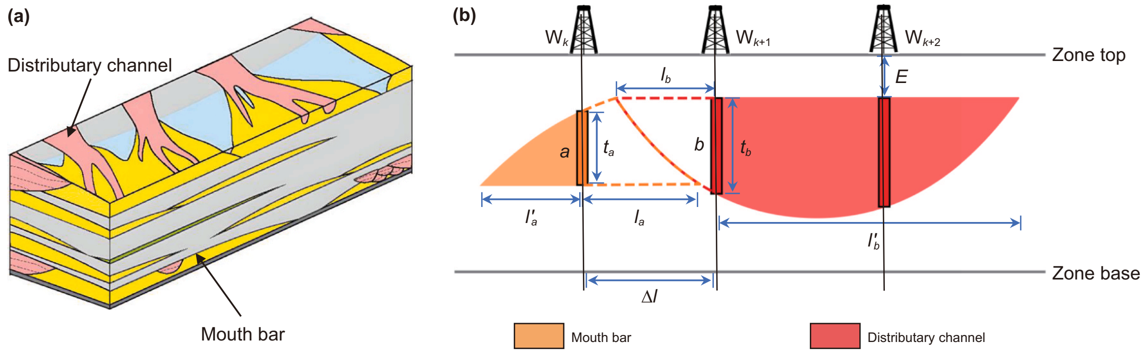

Fig. 3. (**a**) Fan-delta model. (**b**) Stacking relationship between the mouth bar and distributary channel.

$$p_{\mathrm{E}}(z)=\exp\left(-\frac{(z-\mu_{\mathrm{E}})^2}{2\sigma_{\mathrm{E}}^2}\right) \tag{7}$$

2.2.3. Fitting of the absolute scale

The absolute scale describes the geometric length characteristics of an individual sand body. When the distribution range of a sand body is excessively large, it may represent a composite sand body of different hierarchical levels. The cross-provenance direction extension lengths of sand bodies containing a and b are assumed to follow normal distributions, with probability density functions denoted $f_{\mathrm{L},a}$ and $f_{\mathrm{L},b}$ and cumulative distribution functions $F_{\mathrm{L},a}$ and $F_{\mathrm{L},b}$, respectively. Note that during the section characterization process, the lengths of a and b already characterized between wells are l'_a and l'_b, respectively (Fig. 3(b)). At this stage, the posterior probability density functions for the interwell extension lengths l_a and l_b of the sand bodies containing a and b can be obtained using Bayesian probability:

$$g_{\mathrm{L},a}(l_a)=\begin{cases}F_{\mathrm{L},a}(l'_a), & l_a=0\\ f_{\mathrm{L},a}(l'_a+l_a), & l_a>0\end{cases} \tag{8}$$

$$g_{\mathrm{L},b}(l_b)=\begin{cases}F_{\mathrm{L},b}(l'_b), & l_b=0\\ f_{\mathrm{L},b}(l'_b+l_b), & l_b>0\end{cases} \tag{9}$$

Building upon this, when the conjugate probabilities p_{L} of a and b controlled at a statistical scale are explored, their architectural element types must first be considered. Let the interwell distance be Δl. When the architectural element types of a and b are identical, their conjugation implies that $l'_a+l'_b+\Delta l$ is closer to the true extension length of the sand body than $l'_a+l'_b$ is; thus, p_{L} is expressed as

$$p_{\mathrm{L}}(a,b)=P\left(|l-l'_a-l'_b|>|l-l'_a-l'_b-\Delta l|\right)=P\left(l>l'_a+l'_b+\frac{\Delta l}{2}\right)=1-F_{l_a}\left(l'_a+l'_b+\frac{\Delta l}{2}\right) \tag{10}$$

When their architectural element types differ, their conjugation implies the existence of $l_a>0$ and $l_b>0$ satisfying $l_a+l_b\geq\Delta l$. Therefore, p_{L} can be expressed as

$$p_{\mathrm{L}}(a,b)=P\{l_a+l_b\geq\Delta l\}=\int_0^{+\infty}\int_{\max\{0,\Delta l-l_a\}}^{+\infty}g_{\mathrm{L},a}(l_a)g_{\mathrm{L},b}(l_b)\mathrm{d}l_b\mathrm{d}l_a \tag{11}$$

2.2.4. Fitting of the aspect ratio

The aspect ratio describes the quantitative relationship between the vertical thickness and lateral scale and plays a significant role in guiding the prediction of the lateral extent of a sand body. The thicknesses of a and b are denoted as t_a and t_b, and their aspect ratios are denoted as $R_a\sim N\left(\mu_{R_a},\sigma_{R_a}^2\right)$ and $R_b\sim N\left(\mu_{R_b},\sigma_{R_b}^2\right)$, respectively. From the aspect ratio probability density functions f_{R_a} and f_{R_b}, the probability density functions for the interwell extension length can be derived:

$$\begin{cases}g_{\mathrm{R},a}(l_a)=f_{R_a}\left(l_a;t_a\mu_{R_a},t_a^2\sigma_{R_a}^2\right)\\ g_{\mathrm{R},b}(l_b)=f_{R_b}\left(l_b;t_b\mu_{R_b},t_b^2\sigma_{R_b}^2\right)\end{cases} \tag{12}$$

Notably, $l_a=t_ar_a$ and $l_b=t_br_b$ represent horizontal direction information derived from vertical sand body information; these two types of information are mutually orthogonal and thus always independent. Given the spatial distance Δl between a and b, their conjugation implies the existence of $l_a>0$ and $l_b>0$ satisfying $l_a+l_b\geq\Delta l$. Consequently, the conjugate probability of a and b controlled by the aspect ratio is

$$p_{\mathrm{R}}(a,b)=P\{l_a+l_b\geq\Delta l\}=\int_0^{+\infty}\int_{\max\{0,\Delta l-l_a\}}^{+\infty}f_{\mathrm{R},b}(l_b)f_{\mathrm{R},a}(l_a)\mathrm{d}l_b\mathrm{d}l_a \tag{13}$$

2.2.5. Fitting of the lithology inversion

The lithology inversion result, denoted as S, represents the lithology distribution probability data on the interwell section obtained through seismic inversion techniques. Its values range within [0,1], reflecting the probability of encountering sand at each location on the section. Assume that a threshold ϖ is the probability boundary value dividing the sand and mud regions in S, meaning that regions in S with values greater than ϖ are identified as sand and vice versa as mud. Notably, globally, S often lacks a definitive boundary threshold to accurately distinguish sand and mud regions; ω is an uncertain variable. Therefore, the conjugate probability function $p_{\mathrm{S}}(a,b)$ controlled by lithology inversion data is characterized using the minimum ω (denoted as ω_{S}) such that a and b are geometrically 8-connected within the interwell sand distribution region, which means that $p_{\mathrm{S}}(a,b) = \omega_{\mathrm{S}}$.

This paper employs a boundary tracking algorithm with topological analysis capability under a binary search strategy to solve for ω_{S}, with the process outlined as follows:

1) Denote the minimum and maximum values of S as $S_{\min}$ and $S_{\max}$, respectively; initialize $\omega_1 = S_{\min}$ and $\omega_2 = S_{\max}$.
2) Take $\omega = 0.5(\omega_1 + \omega_2)$. If $0.5(\omega_2 - \omega_1) \le \xi$, the search terminates, setting $\omega_{\mathrm{S}} = \omega$.
3) Track 8-connected boundaries of $S \ge \omega_{\mathrm{S}}$ using the boundary tracking algorithm (Suzuki, 1985).
4) If any connected region links a and b, set $\omega_1 = \omega$; conversely, set $\omega_2 = \omega$.
5) Loop through steps 2)–4) until convergence.

Here, ω_1 and ω_2 are the lower and upper bounds of the binary search, respectively, and $0 < \xi \ll 1$ is the precision of the search algorithm. The implication is that when ω takes the value $\omega_{\mathrm{S}} + \xi$, a and b are disconnected; when ω takes the value $\omega_{\mathrm{S}} - \xi$, they are connected. Clearly, within the precision tolerance, $\forall\omega \in [\omega_{\mathrm{S}}, 1]$ implies disconnection, and $\forall\omega \in [0, \omega_{\mathrm{S}})$ implies connection. Therefore, using ω_{S} to characterize $p_{\mathrm{S}}(a,b)$ is reasonable.

Taking the lithology inversion section in Fig. 4 as an example, its minimum and maximum values are $S_{\min} = 0.16$ and $S_{\max} = 0.92$, respectively. Setting the search precision $\xi = 10\%$, during the binary search, ω takes values of 0.540, 0.350, and 0.445, respectively. Since $0.5(0.540 - 0.350) \le 10\%$, $\omega_{\mathrm{S}} = 0.445$ is ultimately obtained (i.e., $p_{\mathrm{S}}(a,b) = 44.5\%$).

2.3. Inference of interwell architectural element characteristics

This section delineates the distribution of individual architectural elements between wells based on the conjugate probability inferred from multiple knowledge sources described previously. The distribution is characterized primarily by hierarchical level, scale, and morphology. Consequently, the hierarchical division of architectural elements is first conducted to identify well intervals drilled through the same element. The scale of architectural elements is subsequently delineated to determine their interwell extension length and associated uncertainty. Finally, the cross-sectional morphology of architectural elements is characterized, delineating their boundaries under the constraints of the stratigraphic framework.

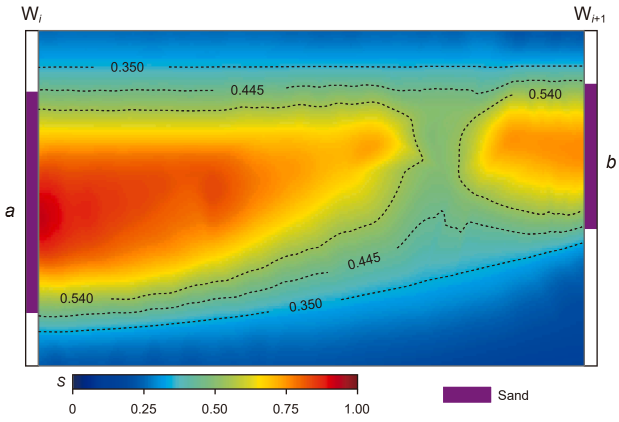

Fig. 4. Schematic diagram of the ω_{S} solving process.

2.3.1. Method for architectural element hierarchical division

Architectural element hierarchical division identifies all the sand segments belonging to the same sand body. The approach involves constructing a comprehensive conjugate probability matrix based on factors influencing conjugate relationships, identifying all conjugate sand body pairs within this matrix using a global optimization search algorithm named the bipartite optimal conjugate pair detection algorithm and partitioning individual architectural elements based on these conjugate pairs.

Consider two adjacent wells, W$_k$ and W$_{k+1}$, drilled through sand segments $\{a_1, a_2, \cdots, a_m\}$ and $\{b_1, b_2, \cdots, b_n\}$, respectively, from shallow to deep within the same chronostratigraphic framework. The method for dividing architectural elements between W$_k$ and W$_{k+1}$ follows the steps below.

(1) Construction of the comprehensive conjugate probability matrix

The comprehensive conjugate probability matrix $\mathbf{P}_{\mathrm{C}}$ integrates the relationship indicator coefficient matrix $\mathbf{C}$, the elevation difference controlled probability matrix $\mathbf{P}_{\mathrm{E}}$, the statistical scale controlled probability matrix $\mathbf{P}_{\mathrm{L}}$, the aspect ratio controlled probability matrix $\mathbf{P}_{\mathrm{R}}$, and the lithology inversion controlled probability matrix $\mathbf{P}_{\mathrm{S}}$. $\mathbf{C}$ is defined by φ:

$$\mathbf{C} = \left(\varphi\left(a_i, b_j\right)\right)_{m\times n} = \begin{pmatrix} \varphi(a_1, b_1) & \varphi(a_1, b_2) & \cdots & \varphi(a_1, b_n) \\ \varphi(a_2, b_1) & \varphi(a_2, b_2) & \cdots & \varphi(a_2, b_n) \\ \vdots & \vdots & \ddots & \vdots \\ \varphi(a_m, b_1) & \varphi(a_m, b_2) & \cdots & \varphi(a_m, b_n) \end{pmatrix} \tag{14}$$

Similarly, $\mathbf{P}_{\mathrm{E}}$, $\mathbf{P}_{\mathrm{L}}$, $\mathbf{P}_{\mathrm{R}}$, and $\mathbf{P}_{\mathrm{S}}$ are defined by p_{E}, p_{L}, p_{R}, and p_{S}, respectively.

$$\mathbf{P}_{\mathrm{E}} = \left(p_{\mathrm{E}}\left(\Delta E_{ij}\right)\right)_{m\times n} \tag{15}$$

$$\mathbf{P}_{\mathrm{L}} = \left(p_{\mathrm{L}}\left(a_i, b_j\right)\right)_{m\times n} \tag{16}$$

$$\mathbf{P}_{\mathrm{R}} = \left(p_{\mathrm{R}}\left(a_i, b_j\right)\right)_{m\times n} \tag{17}$$

$$\mathbf{P}_{\mathrm{S}} = \left(p_{\mathrm{S}}\left(a_i, b_j\right)\right)_{m\times n} \tag{18}$$

where ΔE_{ij} denotes the relative elevation difference between a_i and b_j.

$\mathbf{P}_{\mathrm{C}}$ is constructed via weighted ensemble decision-making. Denoting the weight coefficients as $\beta = (\beta_{\mathrm{E}}, \beta_{\mathrm{L}}, \beta_{\mathrm{R}}, \beta_{\mathrm{S}})$ and the combination matrix as $\mathbf{P}_\beta = (\mathbf{P}_{\mathrm{E}}, \mathbf{P}_{\mathrm{L}}, \mathbf{P}_{\mathrm{R}}, \mathbf{P}_{\mathrm{S}})^{\mathrm{T}}$, the relationship is

$$\mathbf{P}_{\mathrm{C}} = \beta\mathbf{P}_\beta \circ \mathbf{C} \tag{19}$$

where $\circ$ denotes the Hadamard product and β satisfies $\beta_{\mathrm{E}} + \beta_{\mathrm{L}} + \beta_{\mathrm{R}} + \beta_{\mathrm{S}} = 1$.

(2) Determination of conjugate sand body pairs

a_i and b_j are considered a conjugate pair if their comprehensive conjugate probability exceeds a given threshold p_{t}; otherwise, they are not. Crucially, conjugate pairs between two wells exhibit uniqueness, which means that a sand segment in W$_k$ cannot be conjugated to multiple sand segments of the same architectural

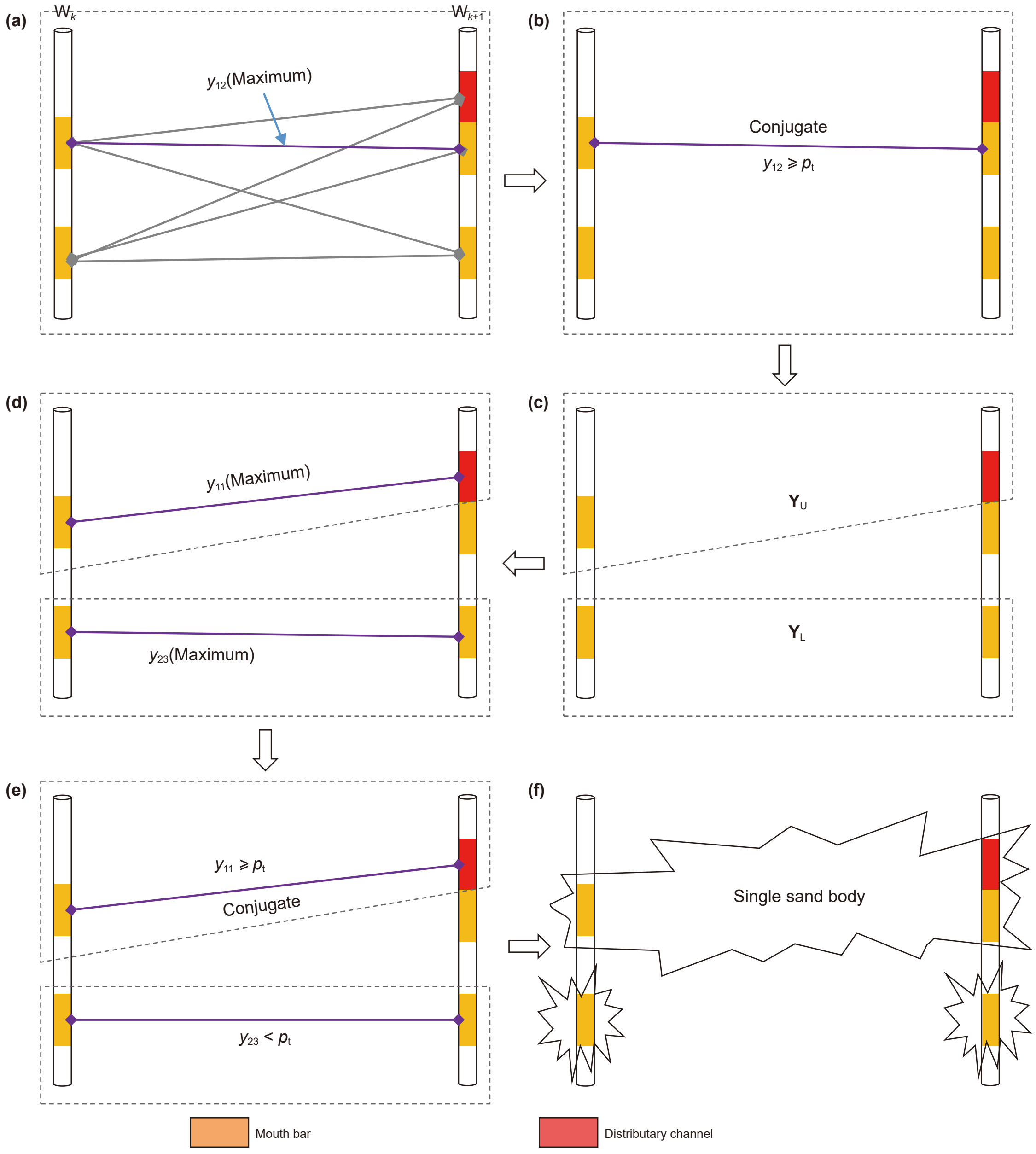

Fig. 5. **(a)** Maximum conjugate probability y_{12} between the first sand body drilled through by W_k and the second drilled through by W_{k+1}. **(b)** y_{12} exceeding the threshold indicates a conjugate relationship between the two sand segments. **(c)** Matrix partitioned into upper and lower submatrices by conjugate pairs. **(d)** Maximum y_{11} in the upper submatrix and maximum y_{23} in the lower submatrix. **(e)** y_{11} exceeding the threshold confirms conjugation between the first sand bodies of W_k and W_{k+1}, with y_{23} below the threshold negating conjugation between the second sand body of W_k and the third sand body of W_{k+1}. **(f)** Transitivity implies that the first and second sand segments of W_k and first sand of W_{k+1} belong to the same individual sand body.

element type in W_{k+1} simultaneously. Therefore, identifying conjugate pairs adheres to the greedy search principle where the pair with the highest conjugate probability is prioritized. This principle is applied iteratively until all possible conjugate pairs are matched.

Conjugate pairs are identified using $\mathbf{P}_\mathrm{C}$ and p_t via the bipartite optimal conjugate pair detection algorithm. The algorithm proceeds as follows.

1) Initialize an empty stack and push matrix $\mathbf{P}_\mathrm{C}$ onto it.
2) If the stack is empty, terminate; otherwise, pop a matrix from the stack, denoted as **Y.** Identify the row index i and column index j of its maximum probability value.
3) If the maximum probability value y_{ij} is less than p_t, a_i and b_j do not form a conjugate pair; otherwise, they form a conjugate pair. In this case, if $i > 1$ and $j > 1$, construct submatrix $\mathbf{Y}_\mathrm{U}$ (U stands for upper) and push $\mathbf{Y}_\mathrm{U}$ onto the stack; if $m > i$ and $n > j$,

construct submatrix $\mathbf{Y}_\mathrm{L}$ (L stands for lower) and push $\mathbf{Y}_\mathrm{L}$ onto the stack.

$$\mathbf{Y}_\mathrm{U} = \left(y_{i'j'}\right)_{(i-1)\times(j-1)} \quad (1 \le i' < i, 1 \le j' < j) \tag{20}$$

$$\mathbf{Y}_\mathrm{L} = \left(y_{i'j'}\right)_{(m-i)\times(n-j)} \quad (i < i' \le m, j < j' \le n) \tag{21}$$

4) Repeat steps 2)–3) until termination.

The conjugate pair detection process illustrated in Fig. 5 provides an example. W_k and W_{k+1} drilled through two and three sand segments, respectively. The algorithm first identifies the pair with the globally highest probability value y_{12} exceeding p_t as the first segment in W_k and the second segment in W_{k+1}. The matrix subsequently splits into $\mathbf{Y}_\mathrm{U}$ and $\mathbf{Y}_\mathrm{L}$. The maximum probability y_{11} in $\mathbf{Y}_\mathrm{U}$ exceeds p_t, confirming the first segment in W_k and the first segment in W_{k+1} as a conjugate pair. Conversely, the maximum probability in $\mathbf{Y}_\mathrm{L}$ is less than p_t, indicating that the second segment in W_k and the third segment in W_{k+1} are not a conjugate pair.

3) Partitioning of architectural elements

The conjugate relationship exhibits transitivity, meaning that sand segments that conjugate to a common segment form conjugate pairs with each other. Consequently, based on the identified conjugate pairs, sand segments sharing conjugate relationships with a common segment are grouped into the same architectural element. As shown in Fig. 5(f), the first segment in W_k and the first and second segments in W_{k+1} are grouped into the same element.

2.3.2. Method for delineating the architectural element scale

Following element partitioning, delineating the interwell extension length of each element is crucial for boundary characterization and uncertainty assessment.

This section primarily predicts the posterior probability density function g_a, g_b of the extension length l_a, l_b for the architectural elements containing a, b. The prediction is achieved by linearly weighting $g_{\mathrm{L},a}$, $g_{\mathrm{L},b}$ and $g_{\mathrm{R},a}$, $g_{\mathrm{R},b}$, constructed earlier, using the weighting coefficient $\alpha = (\alpha_\mathrm{L}, \alpha_\mathrm{R})$ $(\alpha_\mathrm{L} + \alpha_\mathrm{R} = 1)$. Subsequently, l_a, l_b is obtained by sampling from this probability density function.

$$\begin{cases} g_a(l_a) = \alpha_\mathrm{L} g_{\mathrm{L},a}(l_a) + \alpha_\mathrm{R} g_{\mathrm{R},a}(l_a) \\ g_b(l_b) = \alpha_\mathrm{L} g_{\mathrm{L},b}(l_b) + \alpha_\mathrm{R} g_{\mathrm{R},b}(l_b) \end{cases} \tag{22}$$

The uncertainty of the extension length is quantified using the ratio of the potential lateral distribution range to the interwell distance. For a, uncertainty u_a is expressed as

$$u_a(\Delta l, l'_a) = \frac{\min\{D_\mathrm{max}, l'_a + \Delta l\} - \max\{D_\mathrm{min}, l'_a\}}{\Delta l} \tag{23}$$

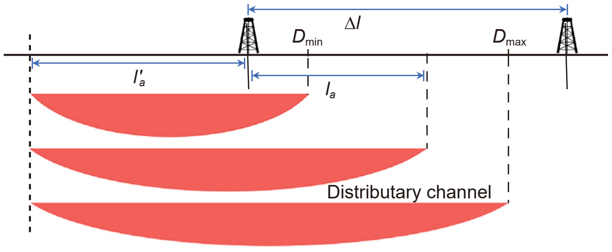

Fig. 6. Schematic diagram of scale uncertainty evaluation.

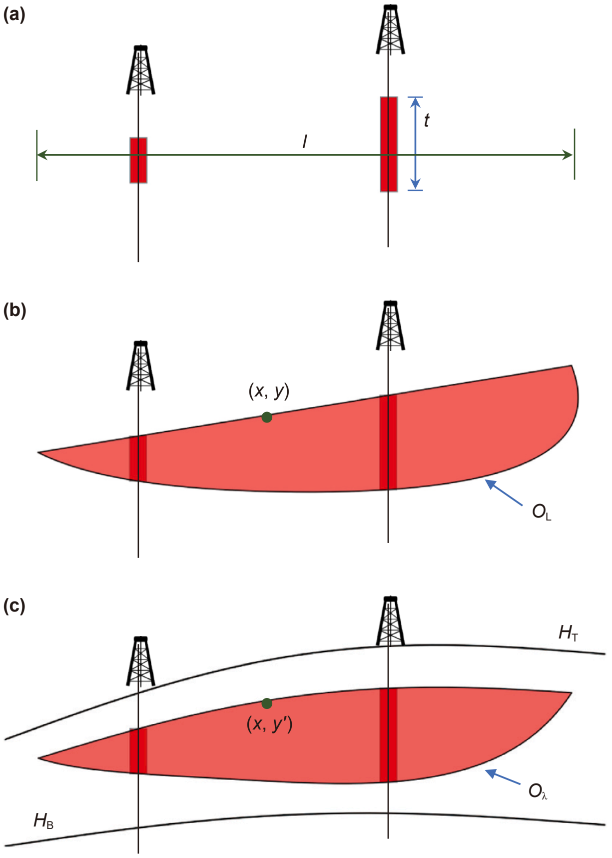

Fig. 7. **(a)** Initial constraint conditions. **(b)** Cross-sectional boundaries of sand bodies characterized only by architectural element types. **(c)** Characterization results refined under stratigraphic constraints.

where D_min and D_max are the minimum and maximum possible extension lengths in the interwell section direction, respectively, derived via function g_a. Fig. 6 illustrates this principle, depicting three scenarios of channel distribution between wells. Scenario 1 shows the shortest interwell extension length D_min, Scenario 3 the longest D_max, and Scenario 2 an intermediate length. The potential distribution range of the channel sand body between the wells is $D_\mathrm{max} - D_\mathrm{min}$.

2.3.3. Method for characterizing architectural element cross-sectional morphology

The cross-sectional boundaries of an architectural element are jointly controlled by the interwell extension length, thickness, morphology, and structural relief. Based on the determined extension length l of individual sand bodies and the thickness t drilled through at each well (Fig. 7(a)), boundaries are characterized under morphological guidance and stratigraphic constraints.

First, parameterize the top and base boundaries of a single sand body based on the extension length l, the thickness t, and cross-sectional morphological characteristics. Although cross-sectional morphologies vary (e.g., flat-top/convex-base, convex-top/flat-base, and lens-shaped), they can generally be characterized using linear or parabolic functions. This study employs linear functions to parameterize flat boundaries (e.g., the top of a distributary channel) and parabolic functions to parameterize curved boundaries (e.g., the base of a distributary channel). Unknown parameters of these linear and parabolic functions are solved under the constraints of length l and thickness t, yielding the parameterized top and base boundaries of the single sand body, as shown in Fig. 7(b).

Subsequently, modify the parameterized boundaries according to structural relief. To account for the influence of structural relief on sand body deposition, an affine coordinate transformation system $\lambda(x)$ is constructed. This system maps the initially fitted sand body boundary O_L (via linear or parabolic functions) onto the structurally constrained sand body boundary O_λ, as illustrated in Fig. 7(c). Implementing this affine transformation requires parameterizing the top and base surfaces of the stratigraphic unit. A piecewise cubic Hermite interpolating polynomial algorithm is introduced for this purpose. Denoting the parameterized top and base surfaces of the isochronous stratigraphic unit as H_T and H_B, respectively, any point $(x, y) \in O_L$ is mapped to point $(x, y') \in O_\lambda$ via the affine transformation system $\lambda(x)$:

$$y' = \lambda(x) = \frac{y}{t}H_T(x) + \frac{t-y}{t}H_B(x) \tag{24}$$

3. Application

This study focuses on an oilfield in the northern Bongor Basin. The Bayesian inference-based expert system method for interwell section architectural element characterization was applied to achieve automated characterization of multiple sections within the study area. The distribution characteristics of the architectural elements in the study area were analyzed based on the characterization results.

3.1. Study area overview

The West African Bongor Basin is located in southwestern Chad, Africa, and has an overall nearly east–west orientation. It is a Mesozoic-Cenozoic continental rift basin formed by dextral strike-slip movement along the Central African Shear Zone. The basin comprises four main structural units: the northern slope, central depression, southern uplift, and southern depression (Li et al., 2024). Most proven hydrocarbon reservoirs in the Bongor Basin are located on the northern slope. The study area, an oilfield within the northern part of the Bongor Basin, covers approximately 14 km^2. The primary reservoirs occur within Cretaceous strata, which can be subdivided from bottom to top into five stratigraphic formations. The lowermost formation is further subdivided into three oil-bearing units. The third oil-bearing unit (Q unit) is subdivided top-down into five sand members: Q_1, Q_2, Q_3, Q_4, and Q_5. The target interval of this study comprises the Q_1 to Q_4 sand members, each of which can be subdivided into four sublayers. The Q unit strata exhibit a variably thickened, aggradational stacking pattern, indicative of a sediment supply dominated by a northern provenance. Depositional systems include fan deltas, nearshore subaqueous fans, and semideep to deep lacustrine deposits. Within fan deltas, distributary channels (dominant microfacies) and mouth bars constitute key architectural elements, manifesting a channel-incised bar complex configuration where active channels persistently erode antecedent bar deposits.

Statistical analysis of the quantitative distribution characteristics of sand bodies along the cross-provenance direction in the study area and adjacent regions reveals the following: Distributary channels exhibit a sinuosity range of 1.1 to 1.2, widths between 100 and 400 m, and aspect ratios of 15–35 in the cross-provenance direction. The relative elevation difference between single sand bodies in distributary channels from different stages is less than 4 m (Table 1). Vertically, they display an upward-fining sequence. Due to incision, they exhibit a “flat top with convex base” morphology in cross-section. Mouth bars have widths of 200–500 m and aspect ratios of 15–35 in the cross-provenance direction, with relative elevation differences between single sand bodies from different stages less than 6 m. Vertically, they display an upward-coarsening sequence. Due to progradation or wave reworking, they exhibit a “flat base with convex top” morphology in cross section.

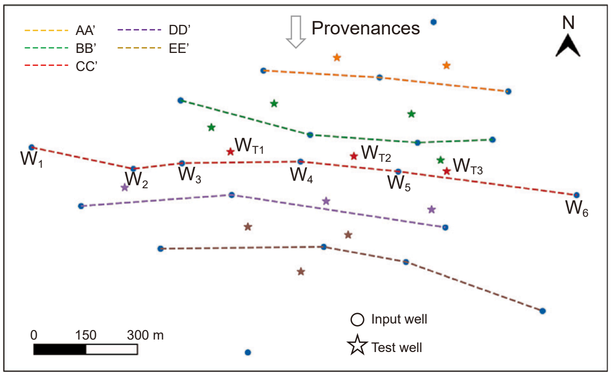

Fig. 8. Distribution map of five cross-provenance direction interwell sections in the study area.

The study area contains 35 development wells with an average well spacing of approximately 350 m. The types of architectural elements drilled through by each well have been identified. A 3D seismic volume (dominant frequency 25 Hz, bandwidth 2–50 Hz) and corresponding lithology inversion volume are available; however, the inversion accuracy is moderate, with the match between the inverted sand distribution and well logs generally below 0.6.

In summary, previous studies have systematically investigated the stratigraphy and reservoirs of the study area. Nevertheless, the complex distribution of architectural elements, the numerous vertical stages, and the inherent difficulty and time-consuming nature of interwell characterization, compounded by subjectivity, lead to variations in results among different geologists. Therefore, there is an urgent need to apply intelligent

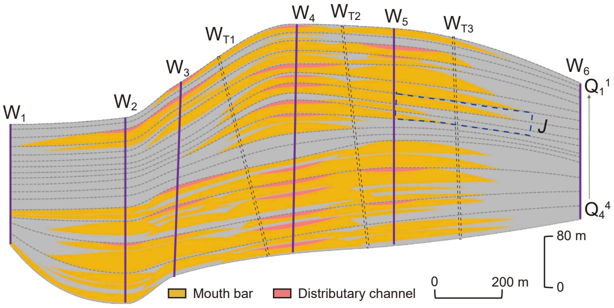

Fig. 9. Fused result of 100 interwell architectural characterizations for the PP' section.

Table 1
Geometric statistical characteristics of the sand bodies in the study area.

Sand body type	Scale, m	Aspect ratio	Relative elevation difference, m
Distributary channel	100–400	15–35	<4
Mouth bar	200–500	15–35	<6

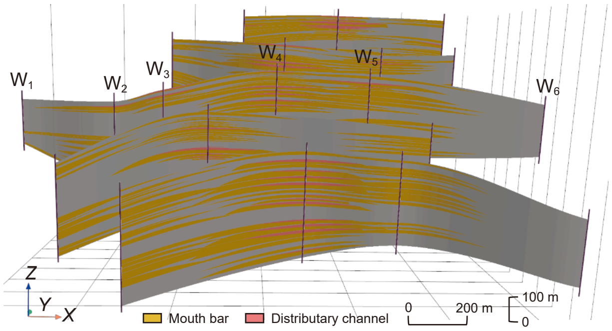

Fig. 10. Characterization results for the five interwell sections in the study area.

characterization techniques to enhance the objectivity, reliability, and efficiency of interwell architectural element characterization.

3.2. Characterization of section architecture

Five cross-provenance interwell sections, marked by different colors in Fig. 8, were selected from the study area. The circular markers on the section lines represent well locations along the section, whereas the differently colored asterisks near the lines represent nearby wells. The input data included interpreted architectural element data from wells, seismic lithology inversion data, stratigraphic horizon data, and the aforementioned statistical characteristics of the study area. Parameters $\alpha = (0.5, 0.5)$, $\beta = (0.25, 0.25, 0.25, 0.25)$, and $p_t = 0.5$ were set, and the interwell section architectural characterization method based on the Bayesian expert system was applied for architectural analysis.

Taking the PP' section in Fig. 8 as an example, the method begins with data parsing; this involves locating the well location information and architectural element interpretation data for the six wells (W_1 to W_6) along this section from the input data and parsing it. The corresponding inversion slice for the interwell section is extracted from the seismic lithology inversion volume. Subsequently, knowledge and data fitting and inference are performed to delineate individual sand bodies and predict their interwell extension lengths, yielding an architectural characterization result for the section. One hundred random characterization runs were conducted for the PP' section, and the results were fused via a mean method to produce a single interwell section architectural characterization result (Fig. 9). The results indicate good section morphology for distributary channels and mouth bars, with thickness variation trends consistent with overall formation thickness changes. Following this procedure, the interwell architectural characterization results for the five sections in the study area are shown in Fig. 10. The computational overhead associated with this approach was evaluated on a standard workstation equipped with an i7-11700KF processor, with each realization requiring approximately 46.39 s, resulting in a total execution time on the order of minutes. This computational cost is considered tractable for practical application, particularly as it enables the quantification of predictive uncertainty—a feature not readily attainable through conventional manual interpretation. The approach thus represents a shift from subjective, labor-intensive drafting toward a more automated and intelligently constrained characterization workflow, indicating its viability and potential scalability for industrial use.

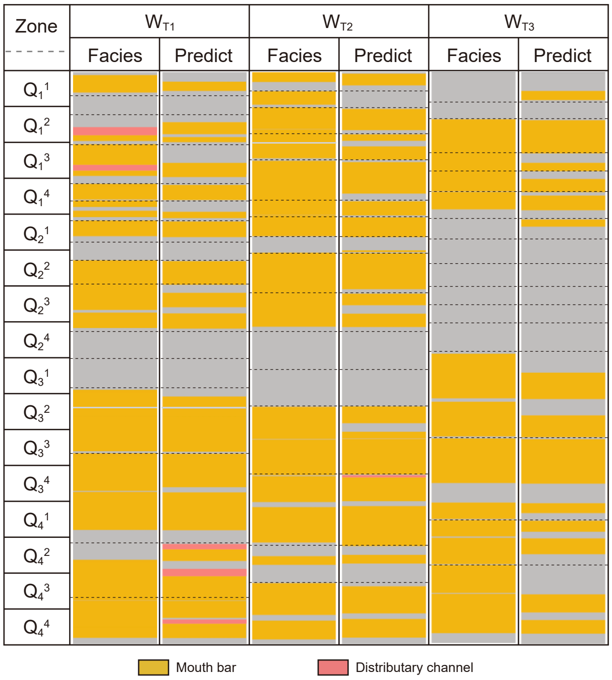

Fig. 11. Comparison of reservoir prediction results with well log interpretations for three blind wells.

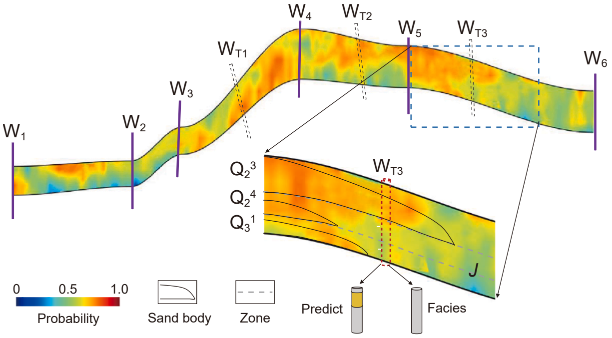

Fig. 12. Constraining effect of seismic inversion data on reservoir prediction.

3.3. Analysis of interwell characterization effectiveness

Blind well tests were conducted using wells adjacent to the interwell sections (marked by asterisks in Fig. 8). The effectiveness of the proposed Bayesian expert system-based method was evaluated by analyzing the match between the interwell characterization results and the actual interpretations at the test wells. Ignoring thickness differences between the actual sand bodies drilled through by the wells and those predicted by the system, the match rate metric is calculated as:

$$\eta_{\mathrm{m}} = \frac{\text{Quantity of matches}}{\text{Quantity of matches} + \text{Quantity of mismatches}} \times 100\% \tag{25}$$

Using the PP' section as an example, adjacent wells W_{T1}, W_{T2}, and W_{T3} were used as test wells and projected onto the section (Fig. 9) to evaluate the characterization effectiveness. The evaluation results for the test wells (Fig. 11) revealed that the number of matching samples for W_{T1}, W_{T2}, and W_{T3} were 34, 29, and 27,

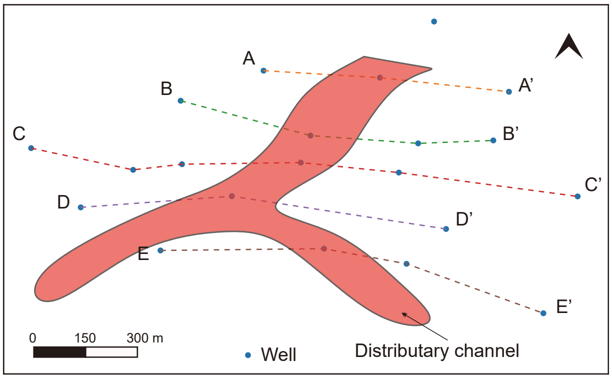

Fig. 13. Planar distribution of distributary channels in the study area.

respectively, with mismatches of 9, 9, and 7, yielding an average match rate of approximately 78.26%.

Evaluating the five sections in this manner yielded an average match rate of approximately 81% between the characterization results and the test well interpretations. A comparison of the characterized architectural elements with those at the test wells reveals two main discrepancies. The first discrepancy is the sand body thickness. Due to the spatial heterogeneity of geological bodies, accurate thickness prediction is often challenging. The second discrepancy is the interwell extent of the sand bodies. Taking region J in the characterization result shown in Fig. 9 as an example, the interwell extent of the two lower sand bodies is well constrained by integrating seismic data (Fig. 12). However, the characterization process must also account for aspect ratio characteristics and uncertainties in the seismic data. Consequently, the upper sand body in region J has a broader predicted extent. While it does not match the sand body at the test well, this interpretation still possesses a degree of geological plausibility.

3.4. *Reservoir architectural characteristics of the study area*

An analysis of the interwell architectural characterization results from the five cross-provenance sections indicates that the target interval sand bodies in the study area are composed of predominantly mouth bars. Mouth bars are concentrated in the central part of the oilfield and exhibit low degrees of lateral migration. Most mouth bars exhibit mound-shaped stacking patterns with significant cumulative thicknesses. Distributary channels exhibit limited development and exhibit primarily ribbon-like patterns on the plane, characterized by long extensions and narrow widths, mainly within the range of 200 to 400 m, as illustrated in Fig. 13. These channels occur as weakly erosional incised fills atop lobe complexes, generating a characteristic channel-bar complex configuration.

Within this distributary channel-bar assemblage style, channels can be classified into deep-incision and shallow-incision types based on their depth of incision into the underlying mouth bars. Channels are classified as deep-incision type when their incision depth exceeds half the thickness of the mouth bar; otherwise, they are classified as shallow-incision type. A comparison of the characterization results from the five sections at varying distances from the provenance reveals that distributary channels in the study area generally exhibit a proximal-deep incision and distal-shallow incision trend, with shallow-incision channels being the dominant type overall.

Furthermore, the juxtaposition relationships and stacking patterns between distributary channels and mouth bars were analyzed. The lateral assemblage types in the study area include single mouth bars, channel-mouth bar juxtaposition, and lateral mouth bar-mouth bar juxtaposition. The vertical stacking patterns include isolated mouth bars separated by muddy barriers, erosional stacking where channels incise into underlying mouth bars, and vertically stacked mouth bars.

4. Discussion

Interwell architectural characterization is a complex process that demands deep integration of specialized geological knowledge and diverse datasets and requires substantial time investment. To address the limitations of existing methods—specifically, their high manual intervention, insufficient automation, and inability to quantify uncertainty in interwell architectural distributions within complex reservoirs—this study proposes an interwell architectural characterization method grounded in a Bayesian inference expert system. This data-knowledge integrated approach synthesizes multisource information (including well information and seismic data), established geometric characteristics of architectural elements, and geological expertise for characterizing reservoir architecture within development well patterns. The results conform to geological principles and demonstrate high concordance (81%) with blind test wells. Critically, the method achieves automated characterization while providing probabilistic distributions of interwell sand bodies based on Bayesian principles; this significantly enhances characterization efficiency and enables robust uncertainty assessment.

The following sections provide a comprehensive evaluation of the proposed method, encompassing its parameter sensitivity and robustness, comparative performance, uncertainty quantification, as well as its limitations and potential for future development.

4.1. *Parameter sensitivity and robustness*

Parameter sensitivity analysis serves as a critical step in validating the reasonableness of parameter settings for a method. The interwell architectural element distribution predicted by the proposed method is significantly influenced by α, β and p_t. Here, α controls the extent to which the lateral extension length of architectural elements relies on different types of scale-related knowledge. β determines the contribution of multiple knowledge sources to the comprehensive conjugate probability $\mathbf{P}_c$. p_t serves as the threshold for conjugate pair identification, directly governing the hierarchical division of sand bodies. These three parameters possess clear geological and mathematical meanings within the model and are mutually independent, thus warranting separate sensitivity analyses.

The parameter $\alpha = (\alpha_L, \alpha_R)$, where $\alpha_L + \alpha_R = 1$, linearly combines the constraints on interwell extension length provided by absolute scale and aspect ratio (see Eq. (22)). As α_L and α_R are independent weight variables following a normal prior distribution, their influence on the predicted extension length can be described by linear relationships where the mean of the extension length is linearly correlated with α_L and α_R, while its variance is linearly correlated with α_L^2 and α_R^2. Given that the mean and variance associated with absolute scale knowledge in the study area are substantially larger than those for aspect ratio knowledge, the mean, representing the geometric scale of architectural elements, and the variance, representing the uncertainty of interwell prediction, of the extension length increase with α_L and decrease with α_R. This trend is confirmed by the normalized mean (orange) and variance (blue) curves in Fig. 14(a). To quantify the impact of α on match rate, 21 groups of α_L values, with corresponding $\alpha_R = 1 - \alpha_L$, were sampled within the interval [0, 1] at a step of 0.05, while β

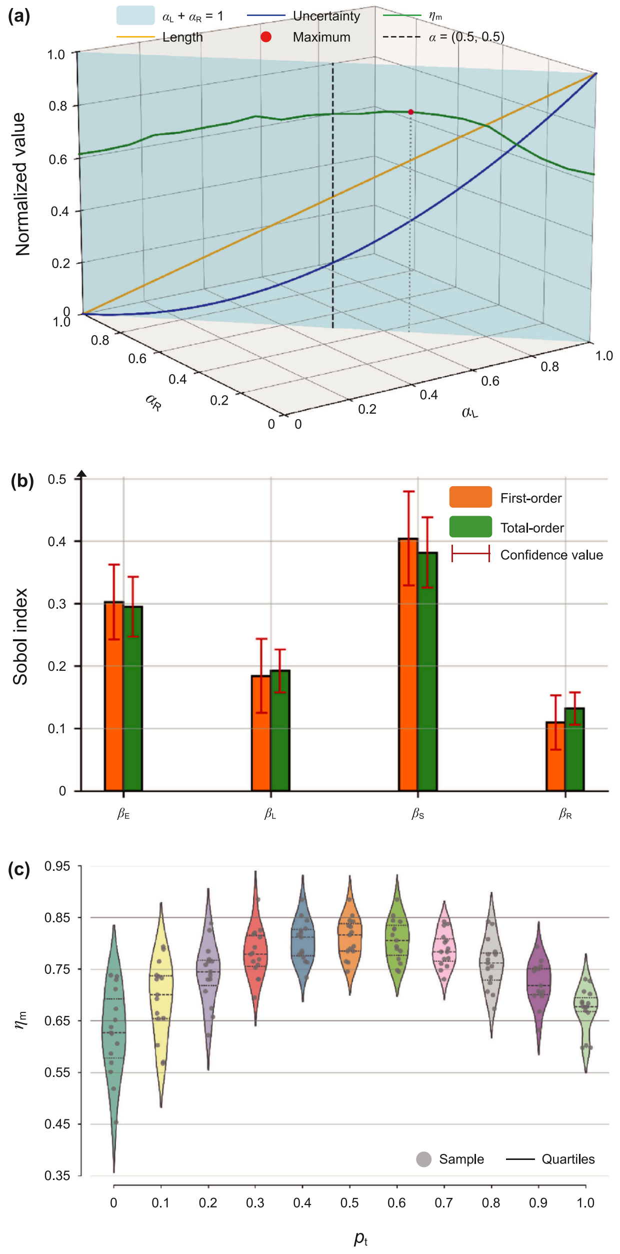

Fig. 14. **(a)** Sensitivity analysis of parameter α, **(b)** sensitivity analysis of parameter β, **(c)** sensitivity analysis of parameter p_t.

and p_t were held constant. Blind well predictions were performed for the five sections, and the average η_m was computed. Results show that η_m exhibits a unimodal pattern, first increasing and then decreasing with increasing α_L, reaching a maximum at $\alpha_L = 0.65$. Notably, even when relying on a single scale knowledge source ($\alpha_L = 0$ or $\alpha_L = 1$), the average η_m for blind wells remains around 0.6, indicating that the model possesses a degree of robustness to the scale prior. However, integrating both knowledge types yields further improvements.

The parameter β directly modulates $\mathbf{P}_C$, making $\mathbf{P}_C$ the target variable for its sensitivity analysis. Given the multidimensional nature of β, the Sobol global sensitivity analysis method is employed. This variance-based decomposition method calculates first-order (S_1) and total-effect (S_T) sensitivity indices to quantify, respectively, the individual contribution of each parameter and its interactions with others to the output uncertainty. One thousand random combinations of β were generated, and their corresponding $\mathbf{P}_C$ values were computed to derive S_1 and S_T for each component (Fig. 14(b)). The results indicate that seismic inversion information provides the strongest constraint on architectural element hierarchy, followed by relative elevation difference. Absolute scale and aspect ratio have comparatively weaker influences. The close agreement between S_1 and S_T suggests negligible interaction effects, implying the contributions from different knowledge sources are approximately additive. Based on the comprehensive evaluation of S_1 and S_T, the order of parameter importance is β_S (0.39), β_E (0.30), β_L (0.19), β_R (0.12).

With α and β fixed, ten experiments were conducted to examine the effect of varying p_t on blind well predictions. As the threshold for conjugate pair acceptance, a lower value makes conjugate sand body pairs more readily accepted, leading to a greater tendency for sand segments from wells to be grouped into the same hierarchical level, whereas a higher value promotes the division of well sand segments into distinct individual sand bodies. As shown in Fig. 14(c), setting p_t to 0 or 1 results in a lower mean and higher variance of η_m, indicating that extreme thresholds cause over-merging or over-splitting, thereby reducing prediction stability. The most robust predictions, characterized by higher mean η_m and lower variance, are achieved when p_t is near 0.5.

Synthesizing the above analyses, the parameter set yielding the optimal η_m in blind well testing for this study area is $\alpha = (0.65, 0.35)$, $\beta = (0.30, 0.19, 0.12, 0.39)$, and $p_t = 0.5$. However, this optimal set is derived from the current blind well test results and is specific to the present study area. For application in new areas, parameters should be set based on their geological interpretation and the perceived reliability of the available knowledge. For instance, if absolute scale knowledge is deemed highly reliable, a higher α_L, greater than 0.5, is warranted. If high resolution seismic data are available, greater weight should be assigned to seismic constraints, effectively increasing β_S. In cases of uncertainty regarding knowledge reliability, parameters can be defined within plausible ranges for stochastic realizations. For the study area in this paper, based on prior geological research that assigns high confidence to all knowledge types, a uniform weighting scheme is also justified—$\alpha = (0.5, 0.5)$ and $\beta = (0.25, 0.25, 0.25, 0.25)$. This choice balances the insights from sensitivity analysis with practical geological consistency and the interpretability of the method.

4.2. Performance and comparative analysis

The characterization of the five interwell sections was conducted using existing methods. A comparative analysis was performed to elucidate the superiority of the method proposed in this study, as summarized in Table 2. Currently, the algorithms capable of characterizing interwell section architecture are primarily three-dimensional architectural modeling methods, such as object-based methods and pixel-based methods.

Among these, object-based methods employ a modeling approach analogous to fitting. This involves first parameterizing the geometric morphology of geological bodies, followed by constructing 3D architectural models by simulating the joint distribution of geological bodies and their properties in three-dimensional space. The Boolean simulation algorithm from this category was applied to build the 3D architectural model shown in Fig. 15(a). The geometric morphology of the architectural units in this model highly conforms to geological patterns, with a conformable cross-sectional morphology and a 100% scale match degree for the simulated geological bodies. However, this method struggles to achieve complete conditioning. Statistics show that the conditioning degree of the simulation results to the well data in the study area is approximately 79%, and the average η_m value at

Table 2
Comparison of methodological characteristics and application performance.

Comparison aspects	Criteria	Boolean simulation	Sequential indicator simulation	BES-IAC (proposed)
Methodological characteristics	Core philosophy	Analogous to fitting	Analogous to interpolation	Analogous to interpolation
	Basic unit	Geobody	Pixel	Interface
	Dimensionality	3D	3D	2D
Application performance	Match rate (η_m)	63.96%	69.35%	81%
	Conditioning degree	79%	100%	100%
	Scale match degree	100%	86%	100%
	Cross-sectional morphology	Conformable	Poor	Conformable

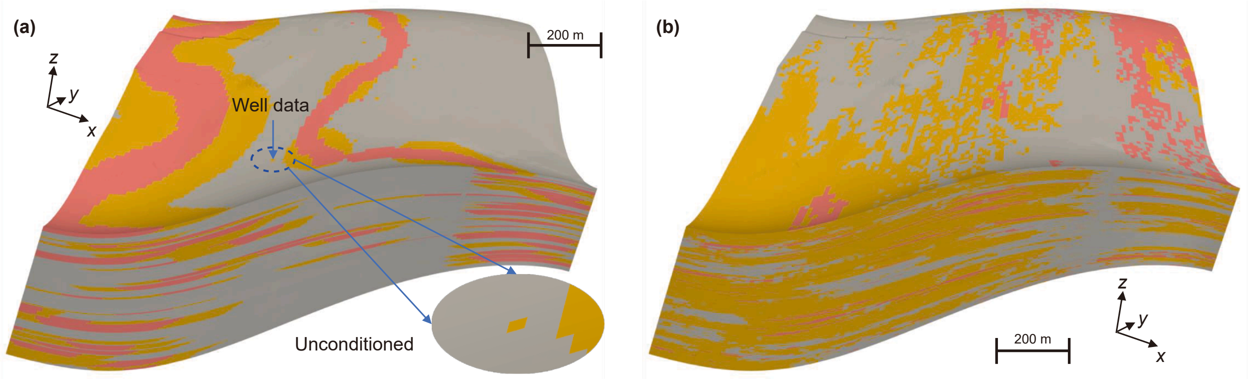

Fig. 15. (**a**) Architectural model constructed using object-based method. (**b**) Architectural model constructed using sequential indicator simulation method.

blind wells across the five sections is only 63.96%. In contrast, pixel-based methods utilize a modeling approach more similar to interpolation. This process begins by quantifying the spatial structure of geological variables through constructing variograms or scanning training images. Reservoir property values are then assigned grid by grid under the guidance of a cumulative conditional probability distribution function. The sequential indicator simulation method from this category was used to construct the architectural model in Fig. 15(b), which achieves a 100% conditioning degree to well data. However, as variograms often inadequately express the spatial structural information of geological bodies—particularly under non-stationary geological conditions—this method performs poorly in depicting spatial morphology. The simulation results appear discrete, with tendencies toward connectivity in some areas. The average η_m value for blind-well predictions across the five sections reaches 69.35%, with a scale match degree for geological bodies of approximately 86%.

The BES-IAC method method proposed in this study shares conceptual commonalities with the two major method categories above. Firstly, it incorporates the object-based concept of parameterizing geological bodies, characterizing architectural interfaces through parameters (Eq. (24)). Secondly, similar to pixel-based methods, it employs a stepwise approach analogous to interpolation, sequentially incorporating well data along the interwell section, constructing individual sand bodies, and iteratively simulating until the scale criteria are met.

Conversely, fundamental differences exist between the proposed method and the two aforementioned categories. Unlike object-based methods, which parameterize geological bodies prior to placement conditioned to well data, the proposed method dynamically parameterizes architectural interfaces while sequentially incorporating well data. This constitutes a dynamic, iterative process for generating the cross-sectional morphology of individual sand bodies, enabling 100% conditioning to well data. Consequently, under conditions of small well spacing, the proposed method demonstrates clear advantages over object-based methods. Unlike pixel-based methods such as multiple-point statistics, which use spatial grid cells as the fundamental simulation units, the proposed method uses architectural interfaces as simulation units. The lateral extension width of these interfaces is simulated by introducing prior normal distributions for scale and aspect ratio, with architectural units then constructed based on these interfaces. This allows for effective control over the morphology and scale of architectural units, enhancing the geological realism of simulation results. Therefore, in scenarios characterized by strong geological non-stationarity, the proposed method shows significant advantages over pixel-based methods.

The proposed method also presents limitations in applicability. The most substantial shortcoming is the current inability to characterize three-dimensional architectural units, a capability

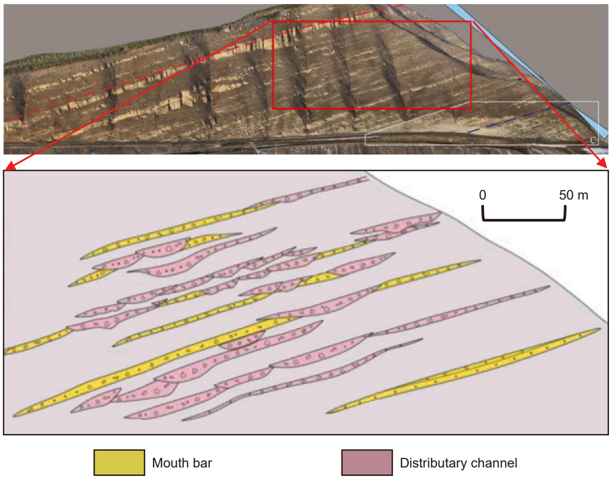

Fig. 16. Outcrop section and its architectural section.

present in existing methods. Secondly, the method is primarily designed for application on sections perpendicular to the provenance direction. On such cross-provenance sections, architectural unit morphology exhibits strong regularity, facilitating the delineation of architectural interfaces under knowledge guidance. Application along sections parallel to the provenance direction remains more challenging.

4.3. Uncertainty interpretation and practical implications

The method generates multiple plausible architectural realizations for a single section and quantifies the associated uncertainty. Uncertainty originates principally from the scale of architectural elements and is governed by aspect ratios and absolute dimension uncertainty. Secondary uncertainty arises from stacking relationships, influenced by relative elevation differences and seismic data limitations.

The magnitude of distribution uncertainty is intrinsically linked to the completeness and quality of available data. Under conditions of poor seismic data quality, uncertainty is governed predominantly by the spacing of the development well. To rigorously evaluate the impact of well spacing on the magnitude of uncertainty, a comparative experiment was designed utilizing an established outcrop profile; this involved generating virtual wells at systematically varied spacings along the profile to analyze the influence of well spacing on the uncertainty of architectural unit characterization outcomes.

A fan delta outcrop within the Lower Cretaceous Xiguayuan Formation of the Luanping Basin, renowned for excellent exposure and typical sedimentary features, was selected. Zhang et al. (2023) meticulously constructed a high-fidelity architectural profile of the outcrop based on field measurements and unmanned aerial vehicle aerial survey data. A representative 350 m × 150 m area within this outcrop was used for experimentation (Fig. 16). This region features a simple tectonic framework with straight bedding planes, internally developed distributary channels and mouth bars. The distributary channels exhibit absolute dimensions ranging primarily from 20 to 100 m, with aspect ratios between 6 and 50, and the relative elevation differences for single sand bodies within the same depositional stage are constrained below 0.6 m. The mouth bar displays a more dispersed range of absolute dimensions, spanning 30 to 160 m, with aspect ratios ranging from 10 to 80, and relative elevation differences for coeval single sand bodies of less than 0.5 m.

Three experimental groups (A, B, and C) were configured to simulate interwell section architectural characterization under distinct well spacing scenarios, defined relative to the average width of the observed channel sand bodies. Group A employed a well spacing of approximately 0.5 times the average channel width (35 m). Group B used a spacing equal to the average width (60 m). Group C implemented a spacing of twice the average width (150 m). For each experiment, the geometric characteristics of the architectural elements and the sand body segments drilled through by the virtual wells served as known input constraints. The proposed method was then applied to stochastically generate multiple realizations of the architectural element distribution along the section. An accuracy metric, defined as the intersection area divided by the union area between the predicted sand body

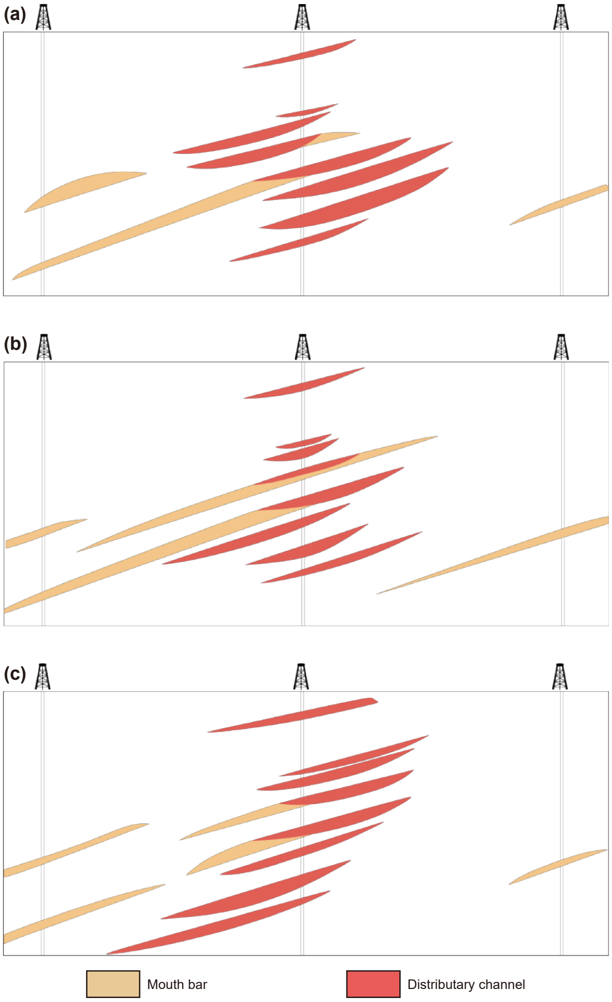

Fig. 18. (**a**) First output from the Group C experiment. (**b**) Second output from the Group C experiment. (**c**) Third output from the Group C experiment.

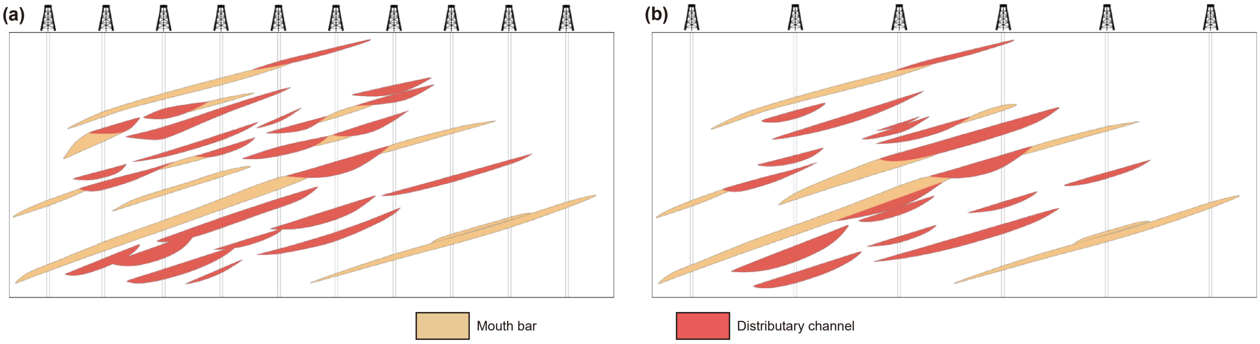

Fig. 17. (**a**) Characterization outcomes from the Group A experiment. (**b**) Characterization outcomes from the Group B experiment.

distribution region $\widehat{\Omega}$ and the actual distribution region Ω observed in the outcrop, was employed for evaluation:

$$\eta_{\mathrm{c}} = \frac{\widehat{\Omega} \cap \Omega}{\widehat{\Omega} \cup \Omega} \times 100\% \tag{26}$$

The experimental results demonstrate distinct uncertainty profiles. In Group A, where the well spacing was generally smaller than the individual channel architectural element widths, adjacent virtual wells frequently drilled through the same channel element, enabling robust boundary definition through dense well control. Consequently, the section characterization uncertainty was minimal, averaging approximately 3.32% for the interwell sand body distribution. Ten stochastic realizations achieved match rates as high as 92.48% between the predicted virtual well and the actual outcrop (Fig. 17(a)). Group B, with well spacing comparable to the average channel element width, resulted in adjacent wells typically drilled through distinct units. While boundaries of large-scale elements drilled through by wells were accurately delineated and connectivity relationships for smaller elements between wells could be inferred, uncertainty increased significantly. The average uncertainty in the interwell sand body distribution reached approximately 23.21%. The highest match rate observed among the one hundred stochastic predictions was approximately 91.22% (Fig. 17(b)). Group C, characterized by well spacing exceeding typical channel element widths, faced substantial difficulty in defining large-scale element boundaries, leading to high distribution uncertainty (53.16%). The method generated diverse realizations that exhibited low similarity (Fig. 18), with the highest match rate among one thousand predictions reaching 89.74%.

The result of group C profoundly reveals the inherent multiplicity of solutions in interwell architectural prediction under sparse well patterns relying on existing geological statistics and seismic data. Under such high-uncertainty conditions, the highly diverse stochastic realizations produced by this method provide a probabilistic, risk-quantifiable planning framework for decision-making in early development stages or data-scarce regions. Specifically, spatial superposition statistics are first conducted on hundreds of equiprobable stochastic realizations to construct a sand body probability model, as shown in Fig. 19. The probability value at any spatial point in this model reflects the confidence level that the point represents effective reservoir. This step is mathematically based on the fundamental principle of Monte Carlo simulation and forms the foundation for all subsequent analyses. Based on this probability model, a hierarchical risk-graded decision strategy can be implemented for ranking drillable targets. Areas with probability values greater than 0.8 can be regarded as confirmed reservoirs, where key production wells of the base well pattern are recommended to be deployed with minimal risk. For fuzzy zones with probability values between 0.3 and 0.8, they should be explicitly planned as priority targets for infill wells, appraisal wells, or logging-while-drilling operations, aimed at acquiring additional information to reduce development risks. In contrast, areas with probability values below 0.1 may be temporarily excluded from the assumption of reservoir continuity in geological interpretation and treated as potential barriers or non-reservoirs in well pattern design.

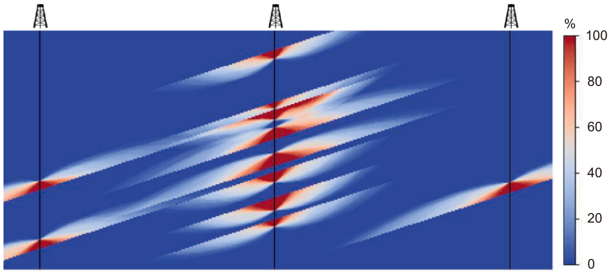

Fig. 19. Sand body probability model for reservoir development decision-making.

4.4. Limitations and future directions

The BES-IAC method proposed in this paper faces significant challenges but also holds considerable potential for further development in terms of transferability and scalability.

On one hand, the BES-IAC method is transferable to other depositional systems. However, it is important to note that the method strongly depends on a well-defined, quantifiable prior knowledge base. The performance demonstrated within the fan-delta system in this study largely benefits from the knowledge base specifically calibrated for that environment. For example, the cross-sectional morphology of distributary channels is defined here as “flat base with convex top”—an assumption clearly not applicable to channels in other depositional systems, such as tidal channels within bidirectional erosion systems. This characteristic constitutes the core constraint for transferring the method, necessitating the systematic reconstruction of corresponding knowledge bases and the adjustment of a series of quantitative parameters. This task requires extensive preliminary studies based on diverse data such as field outcrops, modern sediments, and analogous reservoirs, representing a formidable undertaking.

On the other hand, although the current implementation of BES-IAC is limited to 2D cross-sectional architectural characterization, it holds promise for advancing 3D architectural modeling technology in the following two directions.

The results generated by BES-IAC can serve as critical input for 3D architectural modeling methods. Foundational information for reservoir architectural modeling typically comprises 1D well-based architectural interpretations, 2D representations of dominant architectural element distributions, 2D interwell section architectural characterizations, and 3D seismic data. Prevailing modeling workflows rely predominantly on well interpretations as primary inputs, utilizing seismic trend constraints alongside methods—such as hierarchical simulation, process-based simulation, Gaussian simulation, fractal simulation, multiple-point statistics, or conditional generative adversarial networks (Zhang et al., 2023; Altamar, 2024; Liu et al., 2025)—to construct 3D models. To enhance modeling accuracy, some researchers have introduced 2D constraint information, specifically planar dominant facies distributions and interwell architectural sections. This has led to the development of methods such as sand body modeling constrained by dominant facies (Wu et al., 2025) and adaptive spatial sampling for 3D model reconstruction (Wang et al., 2021). These methods leverage multidimensional information effectively, improving the accuracy of architectural models. It is important to recognize that acquiring high-quality 2D constraint information remains challenging. This study provides an intelligent solution for generating such 2D information, which is crucial for enhancing the geological realism and fidelity of 3D architectural models.

The core concept of BES-IAC possesses the potential to be extended into a 3D geological modeling method. However, achieving this goal requires systematically overcoming several key challenges. First, quantitative geological constraints must be enhanced, for instance, by incorporating knowledge such as planar distribution patterns of sand bodies to better constrain their 2D geometry. Second, the inference dimension must be extended—from the current 1D inference along well pairs to 2D planar inference. This could involve constructing planar graph structures based on well distributions, utilizing planar topological relationships to identify and infer conjugate sand body pairs, and enabling sand body continuity prediction under multi-well linkage. Third, computational efficiency will become a major bottleneck. As model dimensionality and the number of inference nodes increase, the solution space and computational complexity grow exponentially, leading to a significant rise in the computational cost of Bayesian inference.

5. Conclusions

Leveraging interpreted well architectural element data, seismic lithology inversion data, an isochronous stratigraphic framework, and established geological principles, this research establishes an interwell architectural characterization method based on a Bayesian inference expert system framework. By introducing normal distributions to quantify various sources of uncertain knowledge, this work employs Bayesian methods to infer the sectional distribution of architectural elements between wells based on data and knowledge while simultaneously evaluating the distribution uncertainty, thereby achieving intelligent interwell architectural characterization.

The application of the method yielded an 81% concordance rate with blind well interpretations. The results effectively delineate the interwell distribution, cross-sectional morphology, and stacking patterns of diverse architectural element types, having significant implications for improving the efficiency of interwell architectural analysis and advancing 3D reservoir architecture modeling technology.

Acknowledging the present constraint of the method to 2D sections, subsequent research will prioritize its extension into 3D domains.

CRediT authorship contribution statement

De-Gang Wu: Writing – original draft, Validation, Methodology, Formal analysis. **Sheng-He Wu:** Methodology. **Zhen-Hua Xu:** Methodology. **Lei Liu:** Methodology. **Ming-Cheng Liu:** Methodology.

Declaration of interests

The authors declare that they have no known competing financial interests or personal relationships that could have appeared to influence the work reported in this paper.

Acknowledgements

This work was supported by Major Science and Technology Project of China University of Petroleum (Beijing) (Grant No. 2462023YJRC034), and the National Natural Science Foundation of China (Grant Nos. 42202178, 42272110).

References

Altamar, R.P., 2024. Advances in basin modeling using Markov chain: Facies deposition in response to sea level variations and random sequence of geologic processes. Lead. Edge 43 (11), 765–773. https://doi.org/10.1190/tle43110765.1.

Agar, S.M., Li, W., Goteti, R., et al., 2019. Bayesian artificial intelligence for geologic prediction: fracture case study, Horn River Basin. Bull. Can. Petrol. Geol. 67 (3), 141–184. https://doi.org/10.35767/gscpgbull.67.3.141.

Chen, H., 2022. Fine Reservoir Description: Techniques, Current Status, Challenges, and Solutions. Gulf Professional Publishing, Cambridge.

Chen, X.K., Liu, J.Y., Chen, C., et al., 2020. Identifying single sand bodies in meandering river deposits based on subdivision of main architecture elements. Acta Sedimentol. Sin. 38 (1), 205–217. https://doi.org/10.14027/j.issn.1000-0550.2019.011 (in Chinese).

Crepaldi, J.L., de Figueiredo, L.P., Zerilli, A., et al., 2024. Bayesian joint inversion of seismic and electromagnetic data for reservoir lithofluid facies, including geophysical and petrophysical rock properties. Geophysics 89 (3), K1–K16. https://doi.org/10.1190/geo2022-0546.1.

Eliason, S.R., 1993. Maximum Likelihood Estimation: Logic and Practice. Sage Publications, Calif.

Herdian, C., Kamila, A., Budidarma, I.G.A.M., 2024. Studi kasus feature engineering untuk data teks: Perbandingan label encoding dan one-hot encoding pada metode linear regresi. Technologia: Jurnal Ilmiah 15 (1), 93–108. https://doi.org/10.31602/tji.v15i1.13457 (in Bahasa Indonesia).

Huang, W., Wang, J., Chen, H., et al., 2021. Application of multi-wave and multi-component seismic data in the description on shallow-buried unconsolidated sand bodies: Example of block J of the Orinoco heavy oil belt in Venezuela. J. Petrol. Sci. Eng. 205, 108786. https://doi.org/10.1016/j.petrol.2021.108786.

Ibekwe, K.N., Oguadinma, V.O., Okoro, V.K., et al., 2023. Reservoir characterization review in sedimentary basins. J Energ Res Rev 13 (2), 20–28. https://doi.org/10.9734/JENRR/2023/V13I2259.

Kelly, S., 2006. Scaling and hierarchy in braided rivers and their deposits: Examples and implications for reservoir modelling. Braided Rivers: Process, Deposits, Ecology and Management 36, 75–106. https://doi.org/10.1002/9781444304374.

Kim, K.T., Villa, U., Parno, M., et al., 2023. hIPPYlib-MUQ: A Bayesian inference software framework for integration of data with complex predictive models under uncertainty. ACM Trans. Math Software 49 (2), 1–31. https://doi.org/10.1145/3580278.

Kundu, S.N., 2023. Depositional environments and facies. In: Geoscience for Petroleum Engineers, pp. 79–89. https://doi.org/10.1007/978-981-19-7640-7_6.

Li, W., Yue, D.L., Colombera, L., et al., 2023. A novel method for seismic-attribute optimization driven by forward modeling and machine learning in prediction of fluvial reservoirs. Geoenergy Sci. Eng. 227, 211952. https://doi.org/10.1016/j.geoen.2023.211952.

Li, W., Nie, Z.Q., Du, Y.B., et al., 2024. Hydrocarbon accumulation history in Lower Cretaceous in northern slope of Bongor Basin in Chad, Central Africa. Petrol. Explor. Dev. 51 (1), 141–151. https://doi.org/10.1016/S1876-3804(24)60011-X.

Liu, R., Yue, D.L., Li, W., et al., 2024. Characterization of tight sandstone and sedimentary facies using well logs and seismic inversion in lacustrine gravity-flow deposits. J. Asian Earth Sci. 259, 105897. https://doi.org/10.1016/j.jseaes.2023.105897.

Liu, L., Yue, D.L., Li, W., et al., 2025. A novel stochastic simulation method for sedimentary facies based on the generative adversarial network with a spatially-adaptive conditioning module and comprehensive attention mechanisms. Geoenergy Sci. Eng., 213758 https://doi.org/10.1016/j.geoen.2025.213758.

Miall, A.D., 2022. Stratigraphy: a Modern Synthesis, Chapter 3: Facies Analysis. Springer Textbooks in Earth Sciences, Geography and Environment. Springer, Cham, pp. 91–174. https://doi.org/10.1007/978-3-030-87536-7_3.

Qiao, Y., Qiu, L., Wang, J., et al., 2023. Quantitative architectural anatomy of the meandering fluvial deposits of the Neogene upper Guantao Formation in Zhanhua Sag, Bohai Bay Basin, China. J. Earth Sci. 34 (6), 1861–1872. https://doi.org/10.1007/s12583-020-1361-3.

Rajput, S., Pathak, R.K., 2025. Reservoir Delineation and Characterization. Seismic Exploration to Reservoir Excellence. Springer Nature Singapore, Singapore, pp. 321–394. https://doi.org/10.1007/978-981-96-1293-2_7.

Schulz, P., Wegwarth, O., Giese, H., 2025. Risk expression using likelihood ratios and natural frequencies in Bayesian inference tasks—A preregistered randomized-controlled crossover trial. BMC Med. Educ. 25 (1), 505. https://doi.org/10.1186/s12909-025-06990-6.

Sun, Q.H., Zong, Z.Y., Li, X., 2024. Probabilistic seismic inversion based on physics-guided deep mixture density network. Pet. Sci. 21 (3), 1611–1631. https://doi.org/10.1016/j.petsci.2023.12.015.

Suzuki, S., 1985. Topological structural analysis of digitized binary images by border following. Comput. Vis. Graph Image Process 30 (1), 32–46. https://doi.org/10.1016/0734-189X(85)90016-7.

Wang, L.X., Yin, Y.S., Wang, H., et al., 2021. A method of reconstructing 3D model from 2D geological cross-section based on self-adaptive spatial sampling: a case study of Cretaceous McMurray reservoirs in a block of Canada. Petrol. Explor. Dev. 48 (2), 407–420. https://doi.org/10.1016/S1876-3804(21)60032-0.

Wu, S.H., 2010. Reservoir Characterization and Modeling. Petroleum Industry Press, Beijing (in Chinese).

Wu, D.G., Wu, S.H., Liu, C.N., et al., 2025. A 3D reservoir modeling method with constraint from planar distribution of sedimentary facies. J. China Univ. Petrol. 49 (6), 17–29. https://doi.org/10.3969/j.issn.1673-5005.2025.06.002 (in Chinese).

Xu, W., Duan, Z.Q., Zhao, Z.J., et al., 2020. Quantitative characterization of paleochannel sandbody evolution in dense well net area of He 8th layer of Su 6 block in the Sulige gasfield, Ordos basin. China Sci. Pap. 15 (1), 50–59. https://doi.org/10.3969/j.issn.2095-2783.2020.01.008 (in Chinese).

Yan, B.Q., Zhang, X., Yu, L.M., et al., 2014. Point bar configuration and residual oil analysis based on core and dense well pattern. Petrol. Explor. Dev. 41 (5), 654–662. https://doi.org/10.1016/s1876-3804(14)60078-1.

Yu, X.H., Ma, X.X., Mu, L.X., et al., 2004. Geological Model and Hierarchical Interface Analysis of Braided River Reservoirs. Petroleum Industry Press, Beijing (in Chinese).

Yuan, S.Y., Zhao, Y., Xie, T., et al., 2022. SegNet-based first-break picking via seismic waveform classification directly from shot gathers with sparsely distributed traces. Pet. Sci. 19 (1), 162–179. https://doi.org/10.1016/j.petsci.2021.10.010.

Yue, D.L., Wu, S.H., Liu, J.M., 2007. An accurate method for anatomizing architecture of subsurface reservoir in point bar of meandering river. Acta Pet. Sin. 28 (4), 99–103. https://doi.org/10.7623/syxb200704020 (in Chinese).

Zhang, D., Zhang, H., Ren, Q., et al., 2023. Multiple-point geostatistical simulation of nonstationary sedimentary facies models based on fuzzy rough sets and spatial-feature method. SPE J. 28 (5), 2240–2255. https://doi.org/10.2118/215843-PA.

Zhang, K., Wu, S.H., Xu, Y.J., et al., 2022. Sedimentary characteristics of mouth bar within lacustrine fan delta: Insights from the Lower Cretaceous Xiguayuan Formation of Sangyuan outcrop, Luanping Basin. J. Palaeogeogr. 24 (3), 415–432. https://doi.org/10.7605/gdlxb.2022.03.048 (in Chinese).

Zhang, K., Wu, S.H., Wang, H., et al., 2023. Sedimentary architecture of shallow-water fan-delta front in a lacustrine basin: Sangyuan section of Lower Cretaceous Xiguayuan Formation, Luanping Basin, northeast China. Swiss J. Geosci. 116 (1), 3. https://doi.org/10.1186/s00015-023-00432-5.